and phase rotation due to the diffraction in medium i, ℓ_i is propagation length of medium i and γ_i is propagation coefficient of medium i. α_i and k_i are attenuation coefficient and wave number in medium i, respectively. R_{M13} is a reflection coefficient at the boundary between medium 1 and medium 2, T_{M13} is transmission coefficient from medium 1 to medium 3, and T_{M31} is transmission coefficient from medium3 to medium 1. The effects of the multiple interference are included in these R_{M13}, T_{M13} and T_{M31} as shown in equations (4)-(6).

$$R_{M13} = \frac{R_{12} + R_{23} \cdot \exp(-2\gamma_2 \ell_2)}{1 + R_{12} \cdot R_{23} \cdot \exp(-2\gamma_2 \ell_2)} \tag{4}$$

$$T_{M13} = \frac{(1+R_{12}) \cdot (1+R_{23}) \cdot \exp(-\gamma_2 \ell_2)}{1 + R_{12} \cdot R_{23} \cdot \exp(-2\gamma_2 \ell_2)} \tag{5}$$

$$T_{M31} = \frac{(1+R_{32}) \cdot (1+R_{21}) \cdot \exp(-\gamma_2 \ell_2)}{1 + R_{32} \cdot R_{21} \cdot \exp(-2\gamma_2 \ell_2)} \tag{6}$$

B. *Determination of Thickness of the Specimen*

The thickness of the specimen is an important value in this measurement. How to determine the thickness of the specimen is as follows. V_2/V_0 gives the reflection coefficient at the boundary between the buffer rod and the specimen.

$$\left|\frac{V_2}{V_0}\right| = \frac{|A \cdot ATT_2 \cdot R_{M13} \cdot \exp(-2\gamma_1 \ell_1)|}{|-A \cdot ATT_0 \cdot \exp(-2\gamma_1 \ell_1)|} = |R_{M13}| \tag{7}$$

Here, we assume that $ATT_0 = ATT_2$ because ℓ_2 is small. $|R_{M13}|$ has dips in frequency characteristics. In the frequencies which have a dip, the specimen works like a acoustic matching layer. The relation between the dip frequencies f_d and thickness ℓ_2 are given by

$$f_d = \frac{nV_2}{2\ell_2}, \quad n = 1, 2, \cdots \tag{8}$$

Therefore, we can determine the thickness from the dip frequency, if we know the velocity in the specimen. In this measurement, we use the velocities obtained in the VHF range by the conventional measurement (RF pulse-echo method) [4],[5], and we determine the thickness of the specimen with those velocities.

C. *Determination of the Velocity and Attenuation Coefficient*

In order to determine the velocity and attenuation coefficient, we use a V_3 / V_2. It is expressed by

$$\frac{V_3}{V_2} = \frac{|ATT_3|}{|ATT_2|} \cdot \left|\frac{T_{M13} \cdot R_{34} \cdot T_{M31}}{R_{M13}}\right| \exp(-2\alpha_3 \ell_3) \cdot \exp\{j(-2k_3 \ell_3 + \theta_{TR} + \Delta\theta + \pi)\} \tag{9}$$

It is not easy to derive the closed form of V_2 and α_2, so that we use an expression of V_3 and α_3, which are the velocity and attenuation coefficient of solid reference. Defining the phase term in (9) as

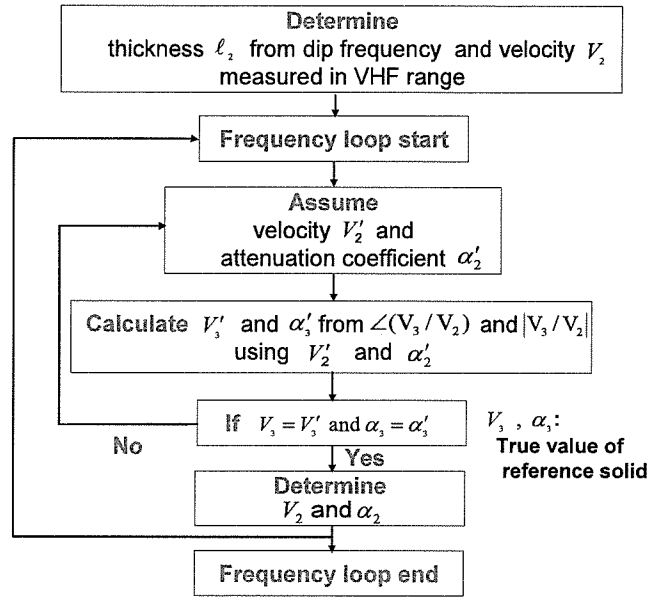

Figure 2. Flow chart of the measurement and calculation.

$$\phi \equiv -2k_3 \ell_3 + \theta_{TR} + \Delta\theta + \pi, \tag{10}$$

V_3 can be obtained from the phase of V_3 / V_2, and α_3 can be obtained from the amplitude of V_3 / V_2 as follows.

$$V_3 = -\frac{2\omega\ell_3}{\phi - \pi - \Delta\theta - \theta_{TR}} \tag{11}$$

$$\alpha_3 = \frac{1}{2\ell_3} \ln\left\{\left|\frac{V_2}{V_3}\right| \cdot \left|\frac{T_{M13} \cdot R_{34} \cdot T_{M31}}{R_{M13}}\right|\right\} - \frac{1}{2\ell_3} \ln\left(\left|\frac{ATT_2}{ATT_3}\right|\right) \tag{12}$$

where $\Delta\theta$ is a phase advance due to the diffraction, and θ_{TR} is a phase change in the specimen. Effects of the diffraction are calculated by Williams' expression [7], [8].

In the right side of equations (11) and (12), V_2 and α_2 are contained. Therefore, we obtain the V_2 and α_2 using an iteration procedure as shown in Fig.2. At first, we determine the thickness of the specimen from the dip frequency of R_{M13} and velocity of the specimen measured in VHF range. After that, we carry out the following procedure for each frequency points. We assume a initial value of the velocity V_2'and attenuation coefficient α_2'. And then, we calculate velocity and attenuation coefficient of reference solid by the equations (11) and (12) using the assumed value. If the calculated values are equal to the true values of the reference solid within the acceptable error, we decide the assumed values are true. If the errors are large, we change V_2'and α_2', and recalculate until the error become negligible.

III. EXPERIMENTS

A. Experimental Setup

Figure 3 shows a useful technique to realize the alignment free measurement. In order to keep the thickness of the liquid specimen and parallelism between the buffer rod and reference solid, we propose a use of spacers like this figure. In this experiment, the spacers are made of ZnO film, which are deposited by RF sputtering on the buffer rod. The thickness of the spacer is approximately 8μm in this experiment. The solid reference is put on the spacers. Using these spacers, we achieve alignment-free equipment. In this experiment, we use a Z-cut α-quarts for the buffer rod and the solid reference, because the attenuation coefficient of α-quartz is small (2.6×10^{-17} s^2/m). The lengths of buffer rod ant reference solid are approximately 8mm and 5mm, respectively.

Figure 4 shows a schematic drawing of measurement chamber. The specimen is put on the ultrasonic device, and reference solid is put on it. A specimen is set between the buffer rod and the reference solid. Weight is used to hold the reference solid on the spacers. Alignment-free is very effective to do a highly stable measurement, as well as making the measurement simplify, because alignment free makes it possible to reduce the size of the equipment. Therefore, it is easy to put them in the small chamber and soaked in a temperature controlled water bath. The temperature of the back side of the reference solid is monitored by thermo couples. It can be kept stable within the variation of ±0.01 °C.

RF pulse signal and complex mode [8] is used in this measurement.

B. Experimental Results

Figure 5 shows a measured V_0, V_2 and V_3 signal, when we measured 25-w% aqueous glucose solution at 23 °C. At the frequencies which have the dip in V_2 signal, the ultrasonic wave passes through the specimen, so that V_3 signal has a peak. While, at the frequencies which have the peak in V_2 signal, the ultrasonic wave reflected at the end of buffer rod, so that V_3 signal has a dip. At the frequencies in which V_3 has a dip, V_3 is too small, and S/N is not enough. Therefore, valid values are obtained only from the regions where V_3 signal has a peak (V_2 signal has a dip).

Figure 6 and Figure 7 show frequency characteristics of velocity and attenuation, respectively for 25-w% aqueous glucose solution and 25-w% aqueous dextran solution at 23 °C. The molecular weight of the dextran is 2,000,000 Dalton. Solid and doted lines show measured value by the conventional measurement. Dots are the value obtained by this method.

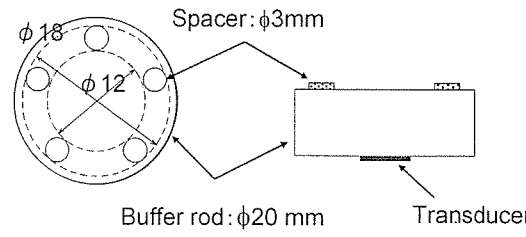

Figure 3. Schematic drawing of spacers on the buffer rod to keep the thickness of the water coupler layer.

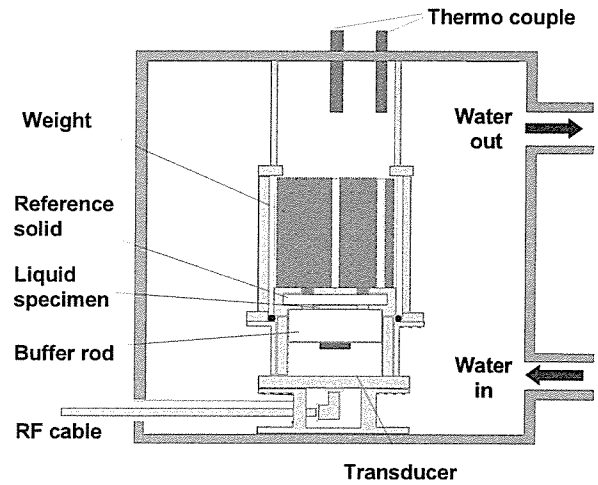

Figure 4. Schematic drawing of measurement chamber.

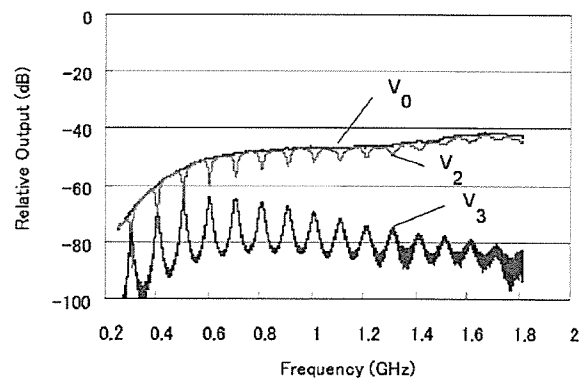

Figure 5. Measured V_0, V_2 and V_3 signal.

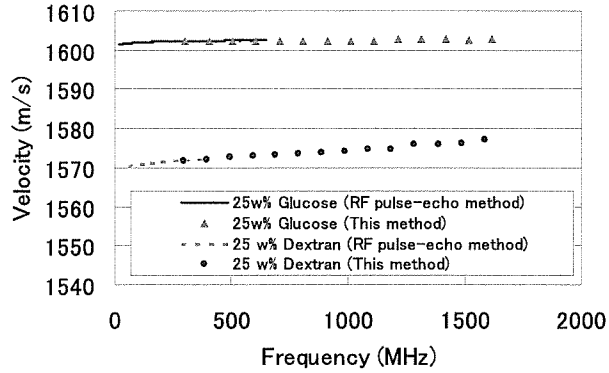

Figure 6. Frequency characteristics of velocity for 25-w%aqueous solution of glucose and 25-w% aqueous solution of dextran at 23 °C.

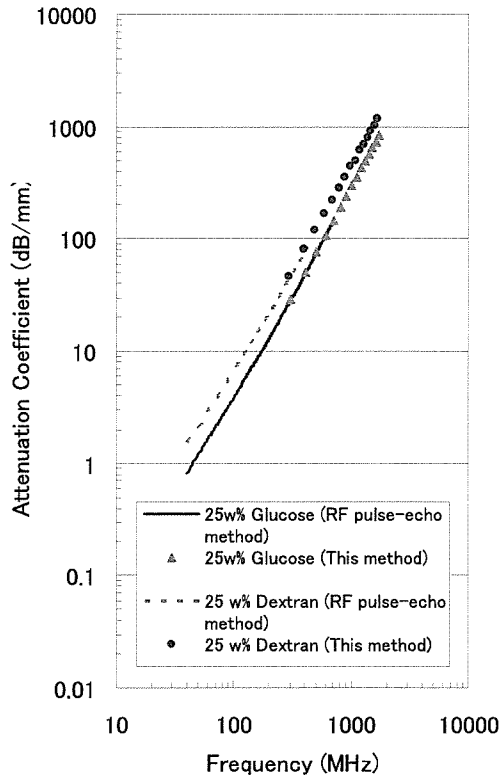

Figure 7. Frequency characteristics of attenuation coefficient for 25-w% aqueous solution of glucose and 25-w% aqueous solution of dextran at 23 °C.

As we can see these experimental results, we can extend the measurement frequency range by the multiple reflection method.

IV. Conclusions

High frequency measurement of acoustic properties for liquid specimens by multiple interference method is proposed. 25-w% aqueous glucose solution and 25-w% aqueous dextran solution was measured approximately from 300MHz to 1.7GHz successfully. This method is very useful to measure the velocity and attenuation coefficient for liquid specimen in UHF range.

References

[1] J. Kushibiki, N. Akashi, T. Sannomiya, N. Chubachi, and F. Dunn, "VHF/UHF range bioultrasonic spectroscopy system and method," IEEE Trans. Ultrason., Ferroelect., Freq. Contr., vol. 42, 1995, pp. 1028-1039.

[2] N. Akashi, J. Kushibiki, N. Chubachi, and F. Dunn, "Acoustic properties of selected bovine tissues in the frequency range 20 to 200 MHz," J. Acoust. Soc. Am, vol. 98, 1995, pp. 3035-3039.

[3] N. Akashi, J. Kushibiki, and F. Dunn, "Acoustic properties of segg yolk and albumen in the frequency range 20 to 400 MHz," J. Acoust. Soc. Am, vol. 102, 1997, pp. 3774-3778.

[4] N. Akashi, J. Kushibiki, and F. Dunn, "Measurement of acoustic properties of aqueous dextran solutions in the VHF/UHF range," Ultrasonics, vol. 38, 2000, pp. 915-919.

[5] N. Akashi, J. Kushibiki, and F. Dunn, "Frequency dependence of acoustic properties of aqueous glucose solutions in the VHF/UHF range," J. Acoust. Soc. Am, vol. 116, 2004, pp. 539-544.

[6] M. Arakawa and J. Kushibiki, "Measurements of acoustic properties of thin lossy specimens using the reference solid specimen in the VHF/UHF rages," in *Rep. Spring Mtg. Acoust. Soc. Japan*, Mar. 2003, pp.965-967.

[7] A. O. Williams, Jr., "The piston source ate high frequencies," J. Acoust. Soc. Amer., vol. 23, 1951, pp.1-6.

[8] J. Kushibiki and M. Arakawa, "Diffraction effects on bulk-wave velocity and attenuation measurements," J. Acoust. Soc. Amer., vol. 108, 2000, pp. 564-573.

High-Frequency Ultrasound Imaging of the Eye with Annular Arrays

Jeffrey A. Ketterling, Jonathan Mamou and Ronald H. Silverman
Riverside Research Institute
Frederic L. Lizzi Center for Biomedical Engineering
New York, New York

Abstract— **High-frequency annular arrays allow for an improved axial depth of field versus single-element, focused transducers. Two piezopolymer-based annular arrays were designed with five, equal-area annuli to operate at 40 MHz and 17 MHz. The 40-MHz array was used for anterior-segment ophthalmic imaging; the 17-MHz array was used for full globe, anterior- and posterior-segment ophthalmic imaging. Digitized radio-frequency data were acquired for all 25 transmit-to-receive ring pairs and the data were then processed with a synthetic-focus algorithm to create a composite image consisting of a series of focal zones. The array performance was validated with a wire phantom and then scans were acquired *ex vivo* from a human eye-bank eye. The synthetically focused B-mode images showed a significant improvement in image quality versus images from a single-element transducer.**

I. Introduction

Current high-frequency ultrasound (HFU, > 15 MHz) imaging transducers are single-element, focused devices that have a limited axial depth of field (DOF) [1]–[3]. The result is an excellent image quality, but only in the imaging plane near the geometric focus. Array transducers provide a means of improving DOF while still maintaining a fine lateral resolution. However, HFU linear and phased arrays have proven to be technically challenging to build and are still under development as various fabrication and instrumentation obstacles need to be overcome [4]–[6].

Annular arrays provide for an improved -6-dB DOF but without the system and design complexity of a linear array. The arrays can be made flat [7]–[9] or with a spherical curvature [10], [11]. Spherical curvature has the advantage of natural focusing, reduced lateral sidelobes, and requiring fewer elements to achieve a significant improvement in DOF. The main drawback with annular arrays is that the array must be laterally translated in order to form an image. Because the annuli have a similar surface area as conventional HFU single-element transducers, standard fabrication and instrumentation techniques may be employed.

Here we demonstrate the improved image quality achieved with annular arrays. The annular arrays each had five rings but were made with different piezopolymers. One array operated at 40-MHz and was fabricated with a 9-μm polyvinylidene fluoride (PVDF) membrane. The second array operated at 17 MHz and was fabricated with a 25-μm poly(vinylidene fluoride-tetrafluoroethylene) [P(VDF-TrFE)] membrane. The operation of each array was first validated with a wire phantom. Images were then acquired from ex *vivo* samples and synthetically-focused array data were compared to fixed focus examples. Finally, we examined extending the imaging capabilities of the annular array by using coded excitation.

II. Methods

A. Transducer Fabrication

The methods of fabricating the annular arrays were described in [10]. Briefly, an array pattern was formed on a copper-clad polyimide (CCP) film. The film was then bonded to the piezopolymer and pressed into a Teflon tube with a steel ball of the appropriate diameter. The Teflon tube was backfilled with epoxy and left to cure. The final transducer was assembled by separating the Teflon tube from the epoxy plug and mounting the epoxy plug into a UHF connector. Connections to the transducer were made via a printed circuit board having MMCX connectors on one end and a flex circuit connector on the opposite end.

Two five-ring array geometries were used for these studies. The first had a 12-mm geometric focus and a 6-mm total aperture and was built with a 9-μm PVDF membrane [11]. The elements for this transducer had center frequencies of 37 MHz. The second array had a 31-mm geometric focus and a 10-mm total aperture and was built with a 25-μm P(VDF-TrFE) membrane [12]. The elements for this transducer had center frequencies of 17 MHz.

B. Scans

Scans were acquired from a wire phantom and from a human eye-bank eye. The wire phantom consisted of 25-μm diameter wires spaced diagonally in 1-mm lateral and axial steps. The wire-phantom data permitted the axial and lateral beam properties of the array to be characterized. All scans were performed using degassed water or saline as the coupling medium. An experimental system under control of a custom LabVIEW program permitted the acquisition of radio-frequency (RF) data from all 25 transmit/receive ring pairs [11]. To accomplish this task, five transducer passes were required where one element was pulsed on each pass and the receive echoes were digitized on all five rings simultaneously.

C. Synthetic Focusing

A synthetic-focus algorithm was developed to permit the focus of the annular array to be axially shifted by post-processing the acquired RF data [11]. To focus the array to

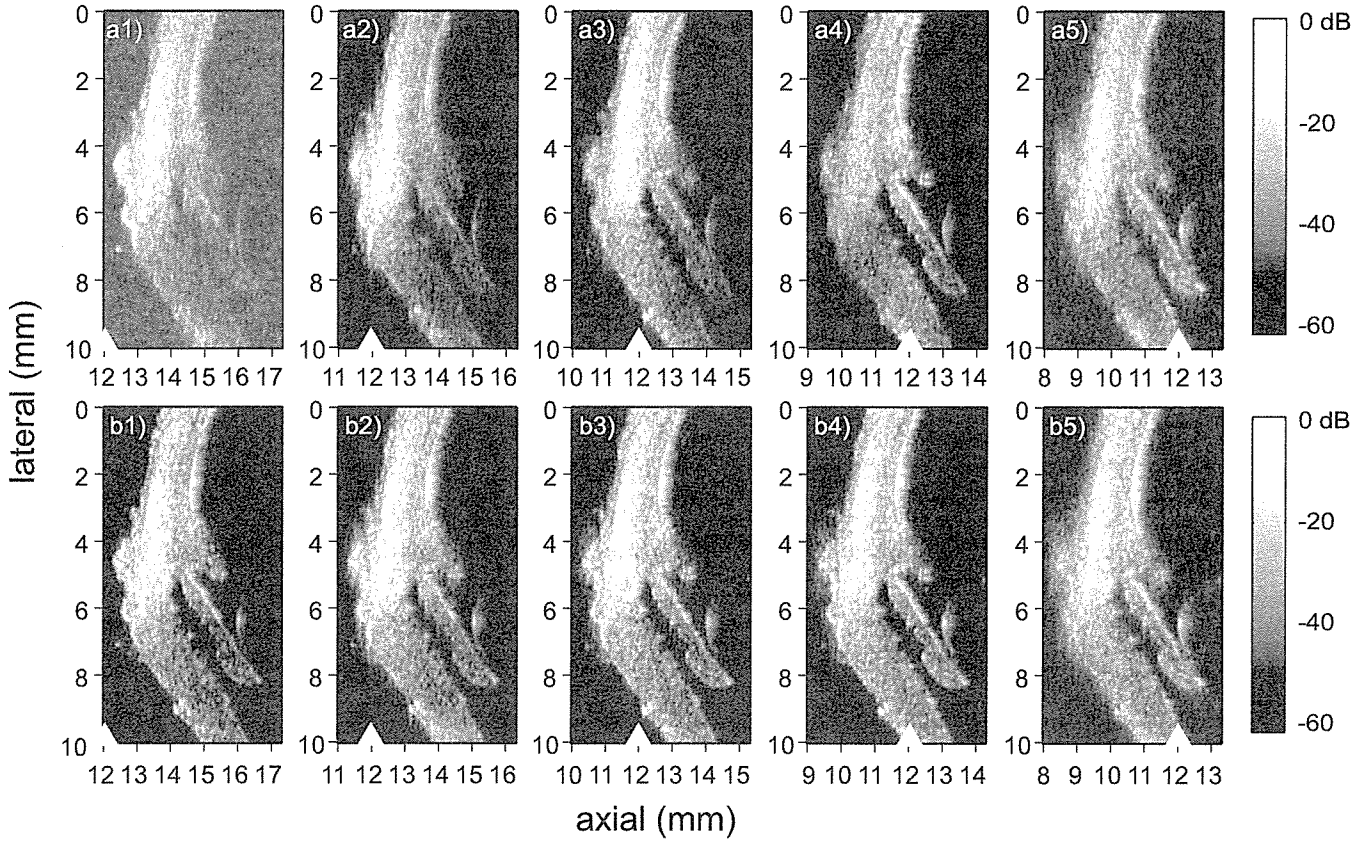

Fig. 1. Series of anterior segment images of a bank eye with the geometric focus (white triangles) progressively incremented in 1-mm axial steps. The top row (a) shows fixed-focus data and the bottom row (b) shows the data after synthetic focusing (geometric focus 12 mm, 41 focal zones, 177 μm/zone).

a depth f on transmit, the time delay, t_n, required for ring n of the array is $t_n = [a_n^2(1/R - 1/f)]/2c$ where R is the geometric focus, c is the speed of sound, and a_n is the average radius of ring n [13]. The round trip delay is then the sum of the transmit and receive delays giving $t^{tot} = t^{\mathrm{T}} + t^{\mathrm{R}}$. To focus at a depth f, t^{tot} is calculated for all 25 transmit/receive pairs. The delays are then applied to the RF A-lines and the resulting signals are summed. In order to increase the DOF over a fixed axial span, f is shifted in intervals of Δf. An overall image is then formed by windowing the data at each focal depth and assembling the windowed data into a final composite image. If the data is processed with $t^{tot} = 0$, the result simulates the case of a single-element transducer having the same total aperture and geometric focus as the annular array.

D. Coded-Excitation

For this study, we extended the capabilities of the annular array using a chirp excitation. A chirp is a coded signal that linearly spans a frequency bandwidth $B = f_2 - f_1$ with f_1 the starting frequency and f_2 the ending frequency. If the chirp sweeps from f_1 to f_2 over a time, T, then the chirp signal is described by $s(t) = w(t)\cos\left(2\pi f_1 t + \pi b t^2\right)$ where $w(t)$ is a windowing function that vanishes outside of $t \in [0, T]$ and b is the sweep rate equal to $(f_2 - f_1)/T$. The role of $w(t)$ is to mitigate the Fresnel ripples present in the chirp spectrum. Theoretically, when the coded signal is a chirp, the SNR improvement is equal to the time-bandwidth product of the chirp [14].

Each received echo signal was compressed before synthetic focusing. Pulse compression was performed by linearly filtering each transmit/receive pair with the compression filter. In theory, the optimal SNR improvement is obtained using the matched filter (i.e., the filter whose impulse response is the time-reversed excitation signal) as the compression filter. However, using this radar-inherited method leads to large-amplitude range sidelobes in compressed signals that degrade the ultrasound image quality [14]. Therefore, in this study, the compression filter was taken to be the matched filter weighted by a Dolph-Chebyshev window (i.e., it was a mismatched filter).

III. Results

A. 40-MHz Array

The 40-MHz array was first characterized with a wire phantom and data were processed with the synthetic-focusing algorithm and with no focusing in order to simulate a fixed-focus transducer. The nominal center frequencies of the array elements were 40 MHz with -6-dB fractional bandwidths of 33%. After impedance matching, the insertion losses of the

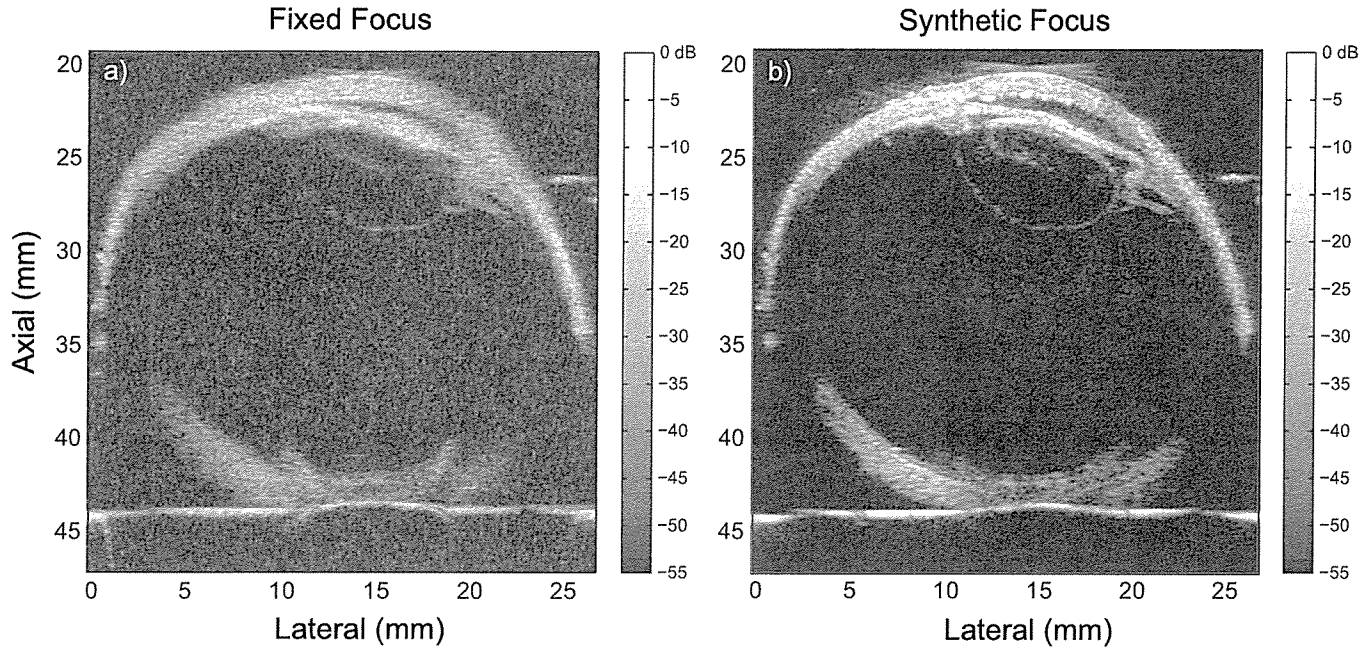

Fig. 2. *Ex vivo* scans of a bank eye with a) fixed focusing and b) with synthetic focusing (geometric focus 31 mm, 41 focal zones, 0.66 mm/zone). The SNRs were (a) 54 and (b) 58 dB.

array elements varied from 29 to 36 dB, increasing from the center to outer annulus.

The improved DOF from using the annular array and the resulting relaxation on the location of the transducer's geometric focus are illustrated in a set of bank eye images (Fig. 1). The figure shows a series of paired images with the top row [Fig. 1(a1 to a5)] representing a fixed focus transducer (summed data with no delay corrections) and the bottom row [Fig. 1(b1 to b5)] representing the same data after synthetic focusing. Each column represents the identical scan plane, but with the geometric focus (white triangles) incrementally placed deeper into the eye in 1-mm steps. The results clearly demonstrate that the geometric focus can be placed within a 4-mm axial range without degrading image quality.

B. 20-MHz Array

The 20-MHz array was also characterized with the wire phantom. The center frequencies of the array elements were all 17 MHz. Insertion losses were 17, 25, 28, 31, and 30 dB from the center to outer ring, respectively. -6-dB fractional bandwidths were 28, 25, 34, 35, and 31% from the center to outer ring, respectively.

Scans of a bank eye are shown for the cases of fixed [Fig. 2(a)] and synthetic [Fig. 2(b)] focusing. The fixed-focus case shows how it is not possible to simultaneously resolve the anterior and posterior segments of the eye. In the synthetically-focused image, the full cross section of the eye is depicted clearly. Features such as the anterior chamber, ciliary body, and a closed iris are visible. Especially interesting is that the entire boundary of the lens is resolved and a cataract can be seen within the lens. With conventional single-element transducers, the lens equator is generally not observed.

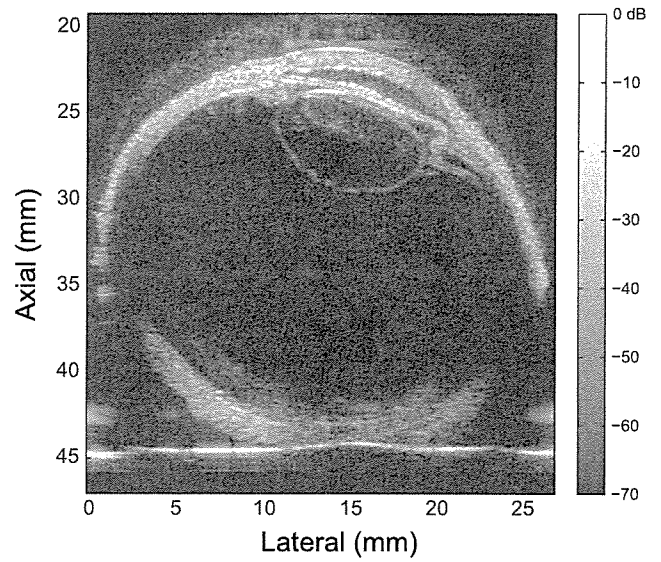

Fig. 3. *Ex vivo* human eye bank scan using coded excitation. The chirp data have been compressed and processed with the synthetic-focusing algorithm (41 focal zones, 0.66 mm/zone). The geometric focus is at 31 mm.

As a final test of the 20-MHz array, a coded-excitation technique was utilized to image the same human cadaver eye plane as shown above (Fig. 3) [15]. The coded-excitation signal consisted of a tapered chirp spanning the frequency range from 5 to 35 MHz over an 8-μs duration. The important point to stress was the additional 15 dB of dynamic range versus the equivalent monocycle images (Fig. 2) and the improved penetration depth. These preliminary results indicate high-frequency coded-excitation is feasible with an annular

array and the results also show how SNR and penetration depth can be improved compared to monocycle pulsing. However, the excitation system is still not fully optimized, which was partly manifested in some axial-sidelobe artifacts seen in Fig. 3.

IV. Conclusion

We have demonstrated that an annular array can be used to drastically improve the -6-dB axial DOF and lateral resolution of HFU ophthalmic imaging. The performance of the annular array was validated with a wire phantom and *ex vivo* scans were acquired from a bank eye. While the current prototype system is not yet sufficiently fast enough for real-time imaging, our preliminary experiments clearly show that annular arrays have clinical utility.

V. Acknowledgements

This work was supported, in part, by the NIH (EY014371, EB000238 and EB006509) and Research to Prevent Blindness.

References

[1] M. D. Sherar and F. S. Foster, "The design and fabrication of high-frequency poly(vinylidene fluoride) transducers," *Ultrason Imag*, vol. 11, pp. 75–94, 1989.

[2] J. M. Cannata, T. A. Ritter, W. H. Chen, R. H. Silverman, and K. K. Shung, "Design of efficient, broadband single-element (20-80 MHz) ultrasonic transducers for medical imaging applications," *IEEE Trans Ultrason Ferroelect Freq Contr*, vol. 50, pp. 1548–1557, 2003.

[3] G. R. Lockwood, D. H. Turnbull, and F. S. Foster, "Fabrication of high frequency spherically shaped ceramic transducers," *IEEE Trans Ultrason Ferroelect Freq Contr*, vol. 41, pp. 231–235, 1994.

[4] T. A. Ritter, T. R. Shrout, R. Tutwiler, and K. K. Shung, "A 30-MHz piezo-composite ultrasound array for medical imaging applications," *IEEE Trans Ultrason Ferroelect Freq Contr*, vol. 49, pp. 217–230, 2002.

[5] J. M. Cannata, J. A. Williams, Q. Zhou, T. A. Ritter, and K. K. Shung, "Development of a 35-MHz piezo-composite ultrasound array for medical imaging," *IEEE Trans Ultrason Ferroelect Freq Contr*, vol. 53, pp. 224–236, 2006.

[6] M. Lukacs, J. Yin, G. Pang, R. C. Garcia, E. Cherin, R. Williams, J. Mehi, and F. S. Foster, "Performance and characterization of new micromachined high-frequency linear arrays," *IEEE Trans Ultrason Ferroelectr Freq Control*, vol. 53, pp. 1719–1729, 2006.

[7] K. A. Snook, C. H. Hu, T. R. Shrout, and K. K. Shung, "High-frequency ultrasound annular-array imaging. part i: Array design and fabrication," *IEEE Trans Ultrason Ferroelect Freq Contr*, vol. 53, pp. 300–308, 2006.

[8] J. A. Brown, C. E. M. Démoré, and G. R. Lockwood, "Design and fabrication of annular arrays for high-frequency ultrasound," *IEEE Trans Ultrason Ferroelect Freq Contr*, vol. 51, pp. 1010–1017, 2004.

[9] E. J. Gottlieb, J. M. Cannata, C. H. Hu, and K. K. Shung, "Development of a high-frequency (> 50 MHz) copolymer annular-array, ultrasound transducer," *IEEE Trans Ultrason Ferroelect Freq Contr*, vol. 53, pp. 1037–1045, 2006.

[10] J. A. Ketterling, O. Aristizábal, D. H. Turnbull, and F. L. Lizzi, "Design and fabrication of a 40-MHz annular array transducer," *IEEE Trans Ultrason Ferroelect Freq Contr*, vol. 52, pp. 672–681, 2005.

[11] J. A. Ketterling, S. Ramachandran, and O. Aristizábal, "Operational verification of a 40-MHz annular array transducer," *IEEE Trans Ultrason Ferroelect Freq Contr*, vol. 53, pp. 623–630, 2006.

[12] J. A. Ketterling, J. Mamou, and R. H. Silverman, "20-MHz annular arrays for ophthalmic imaging," *Proc IEEE Ultrason Symp*, 2006.

[13] M. Arditi, W. B. Taylor, F. S. Foster, and J. W. Hunt, "An annular array system for high-resolution breast echography," *Ultrason Imag*, vol. 4, pp. 1–31, 1982.

[14] T. Misaridis and J. A. Jensen, "Use of modulated excitation signals in medical ultrasound. Part I: Basic concepts and expected benefits," *IEEE Trans Ultrason Ferroelectr Freq Contr*, vol. 52, pp. 177–191, 2005.

[15] J. Mamou and J. A. Ketterling, "Coded-signal imaging using high-frequency annular arrays," *IEEE Ultrason Symp*, 2006 (to appear).

Ultrasonic Imaging and Measurement Toward Noninvasive Tissue Characterization and Evaluation of Physiological Condition of Arterial Wall

Hideyuki Hasegawa, Hiroshi Kanai
Graduate School of Engineering, Tohoku University
Sendai 980-8579, Japan
E-mail: hasegawa@us.ecei.tohoku.ac.jp

Masataka Ichiki
Sendai Hospital of
East Railway Company
Sendai 980-8508, Japan

Fumiaki Tezuka
Sendai Medical Center
Sendai 983-8520, Japan

Abstract— **Ultrasound can be used for mechanical property measurements of the arterial wall in addition to imaging of its morphology. This paper describes accurate imaging of the carotid sinus which cannot be assumed to be a straight cylindrical shell and measurement of elasticity and tissue characterization of the arterial wall based on the motion estimation.**

I. Introduction

Rupture of atherosclerotic plaque is probably the most important factor underlying the sudden onset of the acute coronary syndrome [1]. Direct characterization of the composition and vulnerability of atherosclerotic plaque, rather than measurement of the angiographic lumen [2], may offer insight into the mechanisms of plaque regression and progression [3], [4] and thereby promote evaluation of cholesterol-lowering therapy [5], [6] for reduction of cardiovascular events.

Diagnostic ultrasound is widely used for morphology imaging of the arterial wall. In clinical observation of the carotid artery with ultrasound, it is difficult to accurately image an artery with atherosclerotic plaque or the carotid sinus because they are not flat and ultrasonic beams does not incident normal to the wall in the case of conventional linear scanning. This paper describes a method for accurately imaging such targets by steering ultrasonic beams. For the evaluation of dynamic mechanics, arterial elasticity has been determined by measuring the pulse wave velocity [7] and the rough change in the diameter of the artery [8]. However, the mechanical property of plaque cannot be directly determined by these methods because they evaluate average elasticity of the entire circumference. A method to detect the vulnerability of atherosclerotic plaque with sufficient accuracy has not yet been reported. The purpose of the present study was to determine the regional elasticity of the arterial wall and tissue characterization.

II. Methods

A. Beam steering for accurate B-mode imaging [9]

Figure 1 shows a schematic diagram of the beam steering. The ultrasonic beam scans M positions along the x-axis by conventional linear scanning. The depth of the arterial wall, y_i $(i = 1, 2, ..., M)$, at each beam position, x_i $(i = 1, 2, ..., M)$, is manually predetermined in the B-mode image obtained by conventional linear scanning. The interval between the neighboring ultrasonic beams is defined by $\Delta x = x_{i+1} - x_i$. With respect to each position, (x_i, y_i), of the i-th ultrasonic beam on the wall, a regional slope, $a_{w,i}$, of the arterial wall to the surface of the ultrasonic probe is estimated by the least-squares method using positions, $\{(x_i, y_i)\}$, of neighboring $\pm N$ ultrasonic beams on the arterial wall as follows:

$$a_{w,i} = \frac{(2N+1)\sum_{i=-N}^{N} x_i \cdot y_i - \left(\sum_{i=-N}^{N} x_i\right)\left(\sum_{i=-N}^{N} y_i\right)}{(2N+1)\sum_{i=-N}^{N} x_i^2 - \left(\sum_{i=-N}^{N} x_i\right)^2}. \quad (1)$$

From the estimated $a_{w,i}$, the slope, a_i, and the angle, θ_i, of the beam that is perpendicular to the arterial wall at (x_i, y_i) are determined as follows:

$$a_i = -\frac{1}{a_{w,i}}, \quad (2)$$

$$\theta_i = \tan^{-1} a_i \quad \text{[rad]}. \quad (3)$$

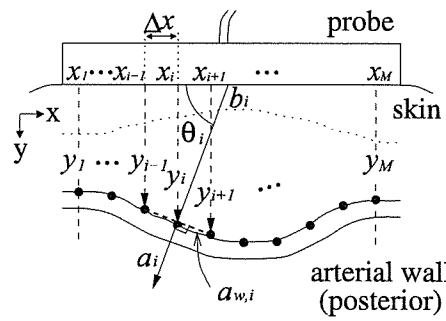

Fig. 1. Determination of optimum beam position and angle ($N = 1$).

From the determined θ_i and the (x_i, y_i) of the arterial wall, the center, b_i, of the the aperture that transmits an ultrasonic beam to (x_i, y_i) is determined as follows:

$$b_i = x_i - \frac{y_i}{\tan\theta_i} = x_i - \frac{y_i}{a_i} \quad \text{[mm]}. \quad (4)$$

By determining θ_i and b_i for all positions, $\{(x_i, y_i)\}$, on the wall, all beams are designed to be perpendicular to the arterial wall.

In this study, θ_i is assigned in discrete values. Therefore, the discrete beam angle, θ'_i, that is nearest to θ_i is selected from preassigned angles of K beams. The b_i of the aperture is calculated again using θ'_i. The b_i of the aperture should be also assigned in a discrete value that depends on the element pitch of the ultrasonic probe. The discrete transmit position, b'_i, of the aperture, which is nearest to b_i, is selected, as well as θ'_i. In this way, the ultrasonic beam is transmitted to the position, (x'_i, y'_i), on the wall as perpendicular as possible. Although the designed ultrasonic beam does not exactly pass through the (x_i, y_i) because of the discrete values of b'_i and θ'_i, the difference, $|x'_i - x_i|$, is less than half the element pitch.

B. Elasticity estimation and tissue characterization based on axial motion estimation

1) Axial motion estimation by the phased tracking method [10]: An ultrasonic beam was sequentially scanned at M positions with a linear-type ultrasonic probe of 7 MHz using conventional ultrasonic diagnostic equipment (Toshiba SSH-140A), and multiple $(N_m + 1)$ points were preset from the luminal surface to the adventitia along the m-th ultrasonic beam $(m = 1, 2, ..., M)$ with constant intervals of h_0 =375 μm at a time t_0 just before the ejection period. By dividing the arterial wall into multiple layers, we defined the n-th layer $(n = 1, 2, ..., N_m)$ as being between two contiguous points, n and $n + 1$, along each beam. For measurement of the change in thickness of each of the N_m layers, the instantaneous depth $x_{m,n}(t)$ of the n-th point along the m-th beam was simultaneously tracked by applying the *phased tracking method* to the received ultrasound. The minute decrease of several tenths of a micrometer in thickness of the n-th layer resulting from the arrival of the pressure wave at the beginning of the ejection period was determined by $\Delta h_{m,n}(t) = x_{m,n+1}(t) - x_{m,n}(t) - h_0$.

2) Strain and elasticity estimation [11]: From the ratio of the maximum decrease in thickness during one heartbeat, $\Delta h_{m,n,\max} = \max_t |\Delta h_{m,n}(t)|$, to the initial thickness, h_0, of the n-th layer, the maximum deformation of the n-th layer was obtained by $\Delta\varepsilon_{m,n,\max} = \Delta h_{m,n,\max}/h_0$. Since the deformation was sufficiently small and was in the linear regime, it showed incremental strain in the radial direction. By assuming that the arterial wall is incompressible and that the blood pressure is applied normal to each layer, the elastic modulus of the n-th layer along the m-th beam, $E_{\theta,m,n}$, is approximately given by

$$E_{\theta,m,n} \approx \frac{1}{2}\left(\frac{\rho_{m,n,0}}{h_0} + \frac{N_m - n + 1}{N_m}\right)\frac{\Delta p}{\Delta\varepsilon_{m,n,\max}}, \quad (5)$$
$$(n = 1, 2, ..., N_m; m = 1, 2, ..., M)$$

where $\rho_{m,n,0}$ is the initial inner radius of curvature of the n-th layer along the m-th beam at time t_0. We assumed that the pressure in the arterial wall decreases linearly with the distance from the intimal side to the adventitia and that the arterial wall is almost isotropic.

For the region with a length of 18 mm ($M = 60$) along the axis of the artery, the regional elasticity $E_{\theta,m,n}$, was estimated on the cross-sectional image. Since the reflected ultrasound was received at a sampling interval of 100 ns (=75 μm along the depth direction) after the quadrature demodulation, we further divided each layer with a thickness of h_0 into 5 points, shifted the initial depth of each layer by 1/5 of h_0 and applied the above procedure to each depth. Thus, $E_{\theta,m,n}$ was estimated at intervals of 75 μm in the depth direction and 300 μm in the longitudinal direction of the arterial wall.

3) Arterial tissue characterization based on elasticity [12], [13], [14]: In this study, an elasticity image is classified using the likelihood function, L_i (i=1: lipid, 2: blood clot, 3: fibrous tissue, 4: calcified tissue), of the elasticity distributions. To obtain the likelihood function of the elasticity distribution of each tissue, the elasticity distribution is translated using the normal distribution to obtain the probability distribution.

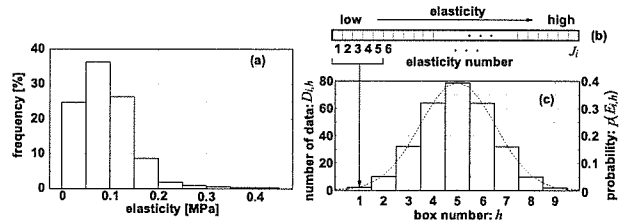

Fig. 2. Illustration of allocation of the elasticity values of the elasticity distribution to the boxes of the normal distribution. (a) The original elasticity distribution of the tissue. (b) The ascending sequence of the elastic modulus of the elasticity distribution. (c) The normal distribution whose number of the boxes corresponding to that of (a).

From *in vitro* experiments, the elasticity distribution of each tissue, i, is obtained as illustrated in Fig. 2(a). The elasticity distribution of each tissue consists of J_i data points with respective elastic moduli (i=1: lipid, 2: blood clot, 3: fibrous tissue, 4: calcified tissue). Using all data of J_i points (J_1: 425, J_2: 301, J_3: 5979, J_4: 579) with respective elastic moduli, the ascending sequence is made for each tissue, i, as shown in Fig. 2(b). In this sequence, the j-th datum (j=1, ..., J_i) has the corresponding elastic modulus, E_j ($E_j \leq E_{j+1}$), where j is named as the elasticity number. It is obviously shown by Fig. 2(a) that the mean elastic modulus of the distribution is largely different from the elastic modulus of the $(J_i/2)$-th datum which is at the center of the ascending sequence. One of reasons for this is considered as follows: To obtain the elastic modulus, the change in thickness (radial strain) of the arterial wall due to the heartbeat is measured with ultrasound. The measured change in thickness is expressed by the sum of the actual change in thickness, Δh, and noise, e, of the measurement system, and the elastic modulus is proportional to the reciprocal, $1/(\Delta h + e)$, of the measured change in thickness [11]. Therefore, the variance of the estimated elastic moduli become large when the actual change in thickness is small (high elastic modulus) in comparison with the case of the large change in thickness (low elastic modulus). As a

result, the elasticity distribution is broadened to the high elastic modulus. Thus, as shown in Fig. 2(c), the normal distribution is assumed with respect to the elasticity number, j, so that the probability around the center of the ascending sequence made becomes highest.

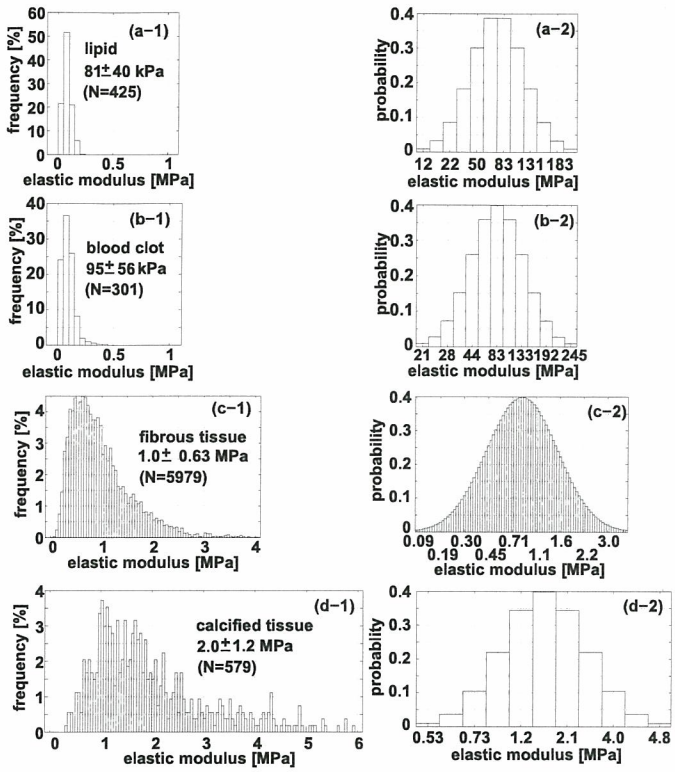

Fig. 3. Elasticity distribution and probability distribution of each tissue. (a) Lipid. (b) Blood clot. (c) Fibrous tissue. (d) Calcified tissue.

The probability distribution of each tissue was obtained by allocating all the data of J_i points of each tissue i to boxes of the normal distribution. The numbers of boxes, $\{B_i\}$, of the normal distributions are determined so that the number of data in the box at a box number, which is located at the triplicate of the standard deviation of the normal distribution from the mean box number, become one. As shown by Fig. 2(c), the number of data, $D_{i,h}$ (h=1, ..., B_i), included in each box is determined by following a line of the normal distribution. Then, the $(J_i/2)$-th datum is included in the box with the highest probability.

By allocating all the data of J_i points of each tissue to boxes of the corresponding normal distribution, the mean elasticity, $\bar{E}_{i,h}$, of the data included in each box is obtained. Figures 3(a-1), 3(b-1), 3(c-1), and 3(d-1) show the elasticity distributions for lipids, blood clots, fibrous tissue, and calcified tissue, respectively, and Figs. 3(a-2), 3(b-2), 3(c-2), and 3(d-2) show the respective probability distributions, $p_i(\bar{E}_{i,h})$, whose horizontal axis was labeled by the mean elasticity, $\bar{E}_{i,h}$, of the corresponding box, $B_{i,h}$.

When the elastic modulus, $E_{m,n}$, measured at depth n along m-th ultrasonic beam is closest to the mean elasticity, $\bar{E}_{i,h}$, of the box, $B_{i,h}$, the probability, $p'_i(E_{m,n})$, with respect to the elastic modulus, $E_{m,n}$, was determined to be $p_i(\bar{E}_{i,h})$.

For each pixel with the corresponding elastic modulus, $E_{m,n}$, the region of interest (ROI), $R_{m,n}$, of ± 450 μm in the depth direction and ± 450 μm in the arterial axis direction is assigned, then there are up to 36 elastic moduli in the ROI. Using the probability distribution, $p'_i(E_{m,n})$, the log likelihood function, $\ln L_i$, for i-th class, is obtained with respect to elasticity values in $R_{m,n}$ as follows:

$$\ln L_i = \sum_{(k,l)\in R_{m,n}} \ln p'_i(E_{k,l}). \qquad (i = 1, 2, 3, 4) \qquad (6)$$

The size of a ROI varies at the edge of an elasticity image. Therefore, we employ the log likelihood function normalized by the number of elasticity values in a ROI. Thus, all pixels in an elasticity image are classified into the class which has the highest likelihood.

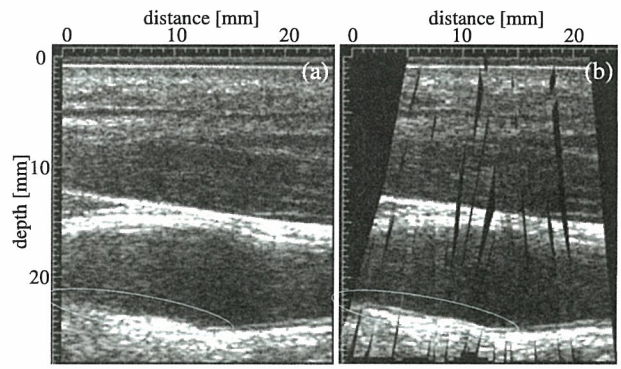

Fig. 4. (a) B-mode image obtained by conventional linear scanning. (b) B-mode image obtained by the proposed method.

III. Experimental results

A. Accurate B-mode imaging of carotid sinus

A human common carotid sinus of a 25-year-old male was measured in the long-axis plane. To reduce the elapsed time for acquiring RF data, ultrasonic beams were transmitted every 5° from $\theta'_1 = 70°$ to $\theta'_9 = 110°$ and discrete steered angles, $\{\theta'_k\}$, were changed frame by frame. Ultrasonic RF data were acquired during 9 frames (82 ms at a frame rate of 110 Hz) just before the time of the R-wave of the electrocardiogram. Figure 4(a) shows a B-mode image obtained by conventional linear scanning, composed of 105 ultrasonic beams with intervals, Δx, of 0.2 mm ($\theta'_5 = 90°$). Figure 4(b) shows a B-mode image constructed from the ultrasonic RF echoes obtained using the calculated beams with $\{(\theta'_i, b'_i)\}$. As shown by the area surrounded by a circle in Fig. 4(a), the intima-media complex cannot be imaged clearly by conventional method in the area where ultrasonic beams is not perpendicular to the wall. However, sufficient reflected echoes were obtained in such an area using the proposed method, and the intima-media complex was almost imaged over the entire scanned area as shown in Fig. 4(b).

B. In vitro elasticity imaging of excised arteries and tissue characterization

Figure 5(a) shows an elasticity image measured *in vitro*, and Fig. 5(b) shows the pathological image of the corresponding section. Lipids, blood clots, and fibrous tissue are indicated by yellow, red, and blue dashed lines, respectively. In Fig. 5(c), the elasticity image was classified using the Mahalanobis distance between a single elasticity value of a pixel and the elasticity distribution of each tissue. In Fig. 6(a), the elasticity image was classified using the likelihood between the elasticity distribution of each small region (not a single pixel) and that of each tissue. In comparison with the classification based on a single elasticity value shown in Fig. 5(c), misclassified regions were reduced using the likelihood function between elasticity distributions as shown in Fig. 6(a). Figure 6(b) shows the tissue classification image obtained by analyzing the pathological image. The pathological image was analyzed as follows: The entire pathological image, which corresponds to the entire elasticity image, is divided into the M sections in the longitudinal direction of the arterial wall, and each m-th section of the M sections is divided into N_m regions in the arterial radial direction. Then, each region is classified into lipids, blood clots, fibrous, and calcified tissues based on RGB values in each region in the pathological image [13]. Regions classified as lipids, blood clots, fibrous tissue, and background were stained yellow, red, blue, and gray, respectively.

The correctness of classification was evaluated by comparing tissue classification images shown in Figs. 5(c) and 6(a) with that in Fig. 6(b) based on the pathological image. Using the likelihood, pixels classified into lipids was found to cluster, and correctly classified pixels were increased (lipids: 32.9%, blood clots: 21.0%, fibrous tissue: 72.8%) in comparison with classification based on a single elasticity value (lipids: 32.9%, blood clots: 17.4%, fibrous tissue: 64.2%).

IV. Conclusion

In this study, methods were proposed for accurate imaging of the carotid sinus which cannot be assumed as a straight cylindrical shell and measuring mechanical properties of the arterial wall based on the motion estimation. Such methods for detailed analysis of the morphology and dynamic mechanics of the artery have potential for providing useful information on diagnosis of atherosclerosis.

References

[1] P. R. Moreno, E. Falk, I. F. Palacios, J. B. Newell, V. Fuster, and J. T. Fallon, "Macrophage infiltration in acute coronary syndromes. Implication for plaque rupture," *Circulation*, Vol. 90, pp. 775–778, 1994.

[2] W. C. Little, M. Constantinescu, R. J. Applegate, M. A. Kutcher, M. T. Burrows, F. R. Kahl, and W. P. Santamore, "Can coronary angiography predict the site of a subsequent myocardial infarction in patients with mild-to-moderate coronary artery disease?" *Circulation*, Vol. 78, pp. 1157–1166, 1988.

[3] H. M. Loree, R. D. Kamm, R. G. Stringfellow, and R. T. Lee, "Effects of fibrous cap thickness on peak circumferential stress in model atherosclerotic vessels," *Circ. Res.*, Vol. 71, pp. 850–858, 1992.

[4] E. Falk, K. Prediman, P. K. Shah, and V. Fuster, "Coronary plaque disruption," *Circulation*, Vol. 92, pp. 657–671, 1995.

[5] G. Brown, J. J. Albers, L. D. Fisher, S. M. Schaefer, J. T. Lin, C. Kaplan, X. Q. Zhao, B. D. Bisson, V. F. Fitzpatrick, and H. T. Dodge, "Regression of coronary artery disease as a result of intensive lipid-lowering therapy in men with high levels of apolipoprotein B," *New Engl. J. Med.*, Vol. 323, pp. 1289–1298, 1990.

[6] J. Shepherd, S. M. Cobbe, I. Ford, C. G. Isles, A. R. Lorimer, P. W. Macfarlane, J. H. McKillop, and C. J. Packard, "Prevention of coronary heart disease with pravastatin in men with hypercholesterolemia," *New Engl. J. Med.*, Vol. 333, pp. 1301–1307, 1995.

[7] P. Hallock, "Arterial elasticity in man in relation to age as evaluated by the pulse wave velocity method," *Arch. Int. Med.*, Vol. 54, pp. 770–798, 1934.

[8] R. H. Peterson, R. E. Jensen, and R. Parnell, "Mechanical properties of arteries *in vivo*," *Circ. Res.*, Vol. 8, pp. 622–639, 1960.

[9] T. Mashiyama, H. Hasegawa, and H. Kanai, "Designing beam steering for accurate measurement of intima-media thickness at carotid sinus," *Jpn. J. Appl. Phys.*, Vol. 45, pp. 4722–4726, 2006.

[10] H. Kanai, M. Sato, Y. Koiwa, and N. Chubachi, "Transcutaneous measurement and spectrum analysis of heart wall vibrations," *IEEE Trans. Ultrason. Ferroelect. Freq. Contr.*, Vol. 43, pp. 791–810, 1996.

[11] H. Hasegawa, H. Kanai, N. Hoshimiya, and N. Chubachi, "Evaluating the regional elastic modulus of a cylindrical shell with nonuniform wall thickness," *J. Med. Ultrason.*, Vol. 31, pp. 81–90, 2004.

[12] H. Kanai, H. Hasegawa, M. Ichiki, F. Tezuka, and Y. Koiwa, "Elasticity imaging of atheroma with transcutaneous ultrasound -preliminary study-," *Circulation*, Vol. 107, pp. 3018–3021, 2003.

[13] J. Inagaki, H. Hasegawa, H. Kanai, M. Ichiki, and F. Tezuka, "Construction of reference data for tissue characterization of arterial wall based on elasticity images," *Jpn. J. Appl. Phys.*, Vol. 44, pp. 4593–4597, 2005.

[14] J. Inagaki, H. Hasegawa, H. Kanai, M. Ichiki, and F. Tezuka, "Tissue classification of arterial wall based on elasticity image," *Jpn. J. Appl. Phys.*, Vol. 45, pp. 4732–4735, 2006.

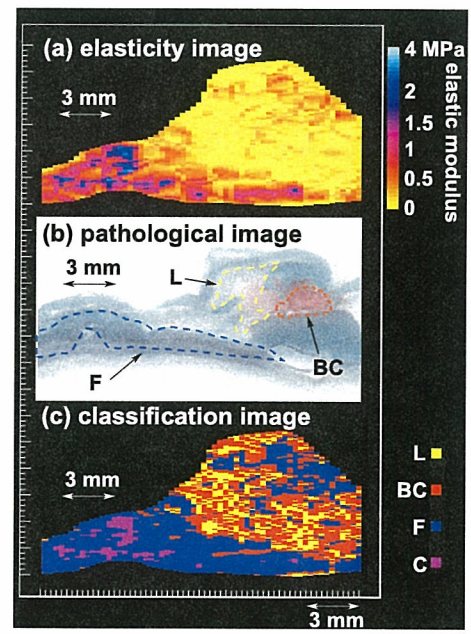

Fig. 5. (a) Elasticity image. (b) Corresponding pathological image. (c) Classification results based on the elasticity value of each pixel.

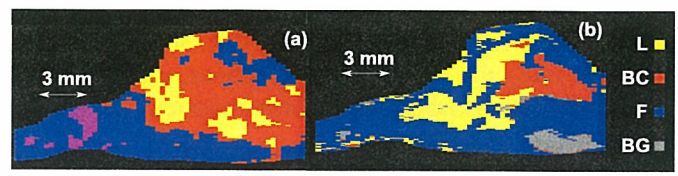

Fig. 6. Classification results based on (a) elasticity distribution of each small region and (b) pathological image.

Multiple Parametric IVUS Imagings for Detection of Vulnerable Plaque

Yoshifumi Saijo, Esmeraldo dos Santos Filho, Tomoyuki Yambe
Department of Medical Engineering and Cardiology
Institute of Development, Aging and Cancer, Tohoku University
Sendai, Japan
saijo@idac.tohoku.ac.jp

Akira Tanaka
Faculty of Symbiotic Systems Science, Fukushima University
Fukushima, Japan

Takahiro Iwamoto, Shuo Li, Makoto Yoshizawa
Graduate School of Engineering, Tohoku University
Sendai, Japan

Abstract— **Detection of vulnerable plaque is important for decision making of the interventional strategy and for understanding pathophysiology of acute coronary syndrome. We have been developing some quantitative evaluation methods of IVUS imaging mainly by analyzing original RF signal. Recently, we have been interested in the region "behind the plaque" because inflammation or neovascularization of adventitia may contribute to the development of atherosclerosis. Clinically, so called "attenuation plaque" is a typical feature of vulnerable plaque. In the present study, we will present multiple parametric IVUS imagings such as conventional IVUS, integrated backscatter (IB), Virtual Histology™ (VH), 1D/2D strain imaging, self-organizing map (SOM), automatic calcium detection and attenuation imaging for visualization attenuation plaques.**

The evaluation of vulnerable plaque by multiple parametric IVUS analyses provides important information for assessment of acute coronary syndrome.

Keywords-intravascular ultrasound (IVUS); parametric imaging; attenuation plaque, vulnerable plaque

I. INTRODUCTION

Intravascular ultrasound (IVUS) has been clinically applied since early 1990's and it has become an important clinical tool for investigation of coronary artery during percutaneous transluminal coronary intervention (PCI) therapies. IVUS is mainly used to measure the luminal and vascular areas and to confirm the full expansion of the coronary stent to the arterial wall. Besides the measurement of dimensions, IVUS also provides important information on tissue character of atherosclerosis.

Recently, many clinical and experimental studies show that the vulnerable plaque in coronary artery is the main cause of acute coronary syndrome. Classical pathological definition of vulnerable plaque is a thin fibrous cap fibroatheroma with infiltration of inflammatory cells. Thus, much attentions have been paid to intimal lesion. However, recent studies have shown that the inflammation or neovascularization in the adventitia are strongly associated with development of vulnerable plaque.

Search for vulnerable plaque in clinical settings becomes very important. The biomarkers such as high sensitivity CRP (C-reactive protein), IL-6 (Interleukin-6) indicating inflammation are used as screening of vulnerable plaque. As IVUS visualizes coronary artery directly, it should provide important information of vulnerable plaque. Clinically, so called "attenuation plaque" is a typical feature of vulnerable plaque. Attenuation plaque is a low echo region without surface high scattering echo and that feature is different from acoustic shadow. Sometimes, it causes "no-reflow" or "slow flow" following PCI. The cause of slow flow may be release of inflamattory cytokines or thrombus by artificial plaque disruption by PCI.

From the point of pathology and clinical experience, we believe that the region "behind the plaque" should be the target of searching vulnerable plaque and we have developed serial parametric IVUS imagings. In the present study, we will present multiple parametric IVUS imagings such as conventional IVUS, integrated backscatter (IB), Virtual HistologyTM (VH), 1D/2D strain imaging, self-organizing map (SOM), automatic calcium detection and attenuation imaging for visualization attenuation plaques.

II. METHODS

A. Recording of RF signal

Commercial available IVUS systems (Galaxy2 or Clear View Ultra, Boston Scientific, USA) were equipped. The central frequency of the IVUS probe (Atlantis SR Pro, Boston Scientific, USA) was 40 MHz and the pulse repetition rate was

7680 Hz. A single frame of the IVUS system consisted of 256 lines so that 7680 pulses made 30 frames per second (f/s). An analogue to digital (A/D) converter board (CompuScope 8500, Gage, USA or DP310, Acqiris, Switzerland) was connected to the RF (radio-frequency signal) output of the IVUS apparatus. The sampling rate was 500 megasamples per second (MSa/s), the resolution was 8-bit and the on-board memory was 128 MB in the Gage A/D board. The sampling rate was 400 megasamples per second (MSa/s), the resolution was 12-bit and the on-board memory was 6 MB in the Acqiris A/D board. Intra-coronary pressure was measured by fluid-filled method using 6 French (2.0 mm) diameter guiding catheter which was inserted into coronary artery.

Biological signals such as electrocardiogram and intra-coronary pressure were simultaneously recorded using an A/D converter (PCI-6024E, National Instruments, USA) with the sampling rate of 100 kSa/s and the resolution of 12-bit. After the RF data were sent to a personal computer, 10 to 80 MHz components of the original RF signal were extracted by using a software-based bandpass filtering method.

Ideally, one frame consisting of 256 lines of the rotational IVUS is equivalent to that of phased-array IVUS. However, a conventional rotating IVUS system uses frame trigger to adjust frame to frame rotational non-uniformity. This indicates the position of the 'n/256'th line is not guaranteed to be at the same position of the previous frame. Then the correlation coefficient between two consecutive matrixes was calculated in the rotational direction and the rotational dis-uniformity was corrected in rotational direction to obtain the maximum correlation coefficient.

B. *Parametric IVUS Imagings*

Serial parametric IVUS imagings are reconstructed from the obtained RF signal. Integrated backscatter (IB) image was produced from the absolute value of time-domain RF signal instead of classical frequency-domain power spectrum of RF signal described in the original IB definition because each power should show same value when the signal was digitized completely. The image of 1D or 2D tissue strain was described in the previous paper [1, 2]. Self-organizing map (SOM) is a neural network that reduces dimensions and display similarities. The shape of power spectra of 256 points of an RF signal was characterized by 18 parameters for SOM [3]. Automatic calcium detection was based on adaptive thresholdngs and high intensity echo with acoustic shadow is defeined as calcium. Virtual Histology™ is also a neural network classification based on power spectrum of RF signal [4]. Attenuation imaging is a preliminary imaging method. The assumption that the total power of transmitted ultrasound from IVUS probe is equal in all direction is the basis of attenuation imaging. The differences of the IB between adjunctive regions of interest on a single IVUS line were considered as uncorrected attenuation coefficient. Then the attenuation coefficient was calibrated as to equalize the total power.

III. RESULTS

A. *Integrated Backscatter*

Figure 1 is a conventional IVUS image reconstructed from RF signal. Figure 2 is the IB image with color of the same region. The resolution is compatible with the sensitivity in conventional IVUS image. The sensitivity is prior to the resolution in IB, however, the image quality seems no difference in this setting.

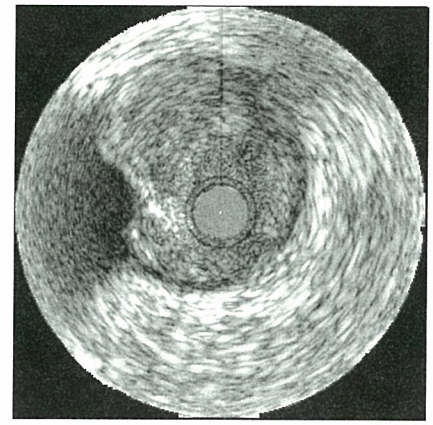

Figure 1. Example of a conventional IVUS image

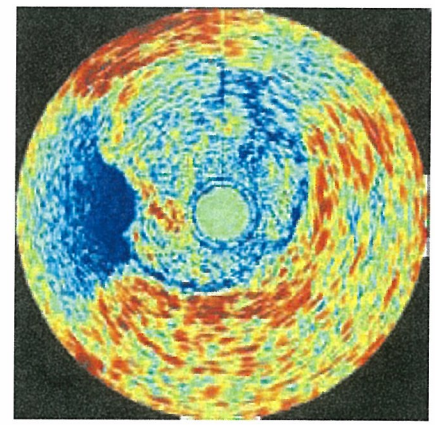

Figure 2. Example of an IB image of the same region of Figure 1

B. *1D Tissue Strain Image*

Figure 3 is 1D tissue strain image of the same region. Dark blue indicates the strain is low and the light blue indicates the strain is high. The region of 10 to 12 o'clock has a high strain that may indicate the soft contents such as lipid.

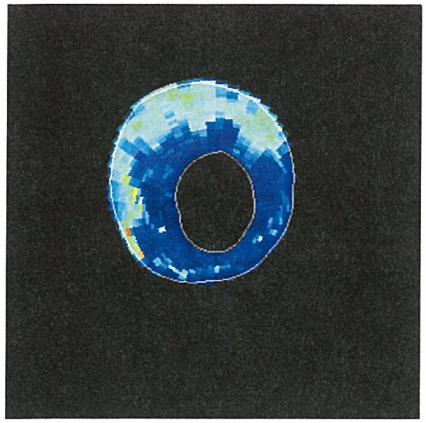

Figure 3. Example of an iD strain image of the same region of Figure 1

C. 2D Tissue Velocity and Strain Images

Figure 4 is 2D tissue velocity and Figure 5 is 2D tissue strain image.

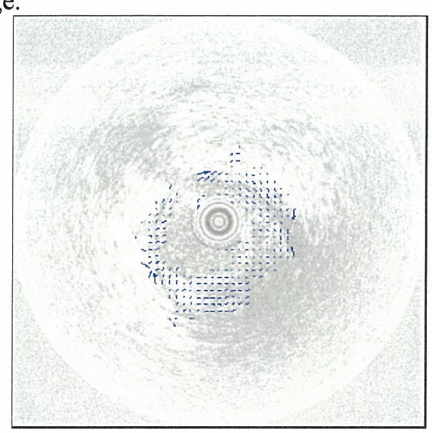

Figure 4. Example of an 2D tissue velocity image

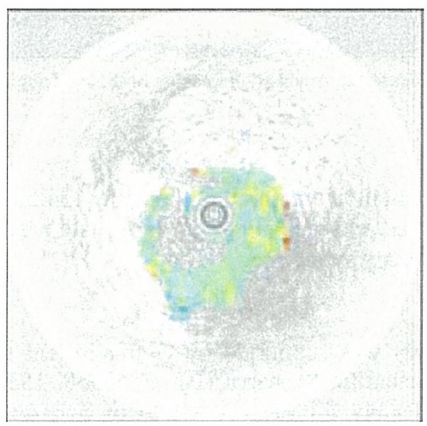

Figure 5. Example of an 2D tissue strain image

D. Virtual Histology™

Virtual HistologyTM classifies the coronary intima into four categories based on a neural network of the power spectra of RF signal. The four categories are fibrous, fibrofatty, calcium and necrotic core. Virmani insists on the necrotic core is the main feature of vulnerable plaque. There are still some discussions on the necrotic core among the clinical cardiologists. Figure 6 is VH image produced by us from the spectral analysis of the RF signal. Figure 7 is the VH image of the same region obtained by commercially available Volcano IVUS apparatus. In both images, outer region at 6 to 9 o'clock shows fibrofatty component while the intima of the same direction shows calcium.

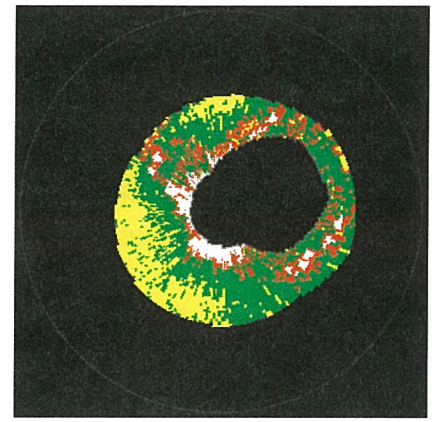

Figure 6. VH image produced by our system.

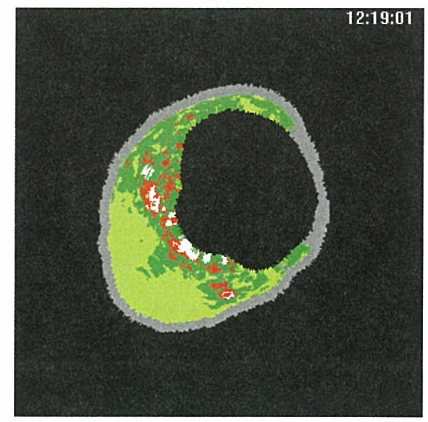

Figure 7. VH image obtained by Volcano IVUS apparatus.

E. Self-organizing Map (SOM)

Figure 8 is an example of SOM image of the same region in Figures 1, 2 and 3. Adventitial side is also classified in the SOM image.

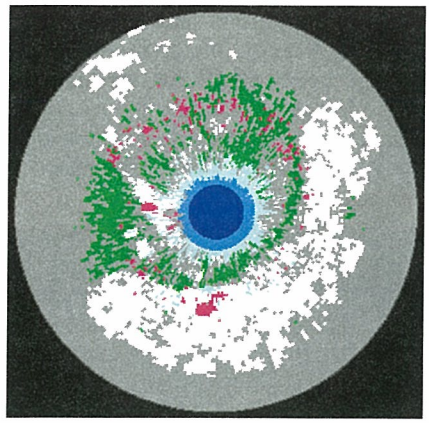

Figure 8. Example of a SOM image

F. Calcium Detection

Figure 9 is an IVUS image of calcification identified manually by three expert medical doctors. Figure 10 is the automatic detection of calcium.

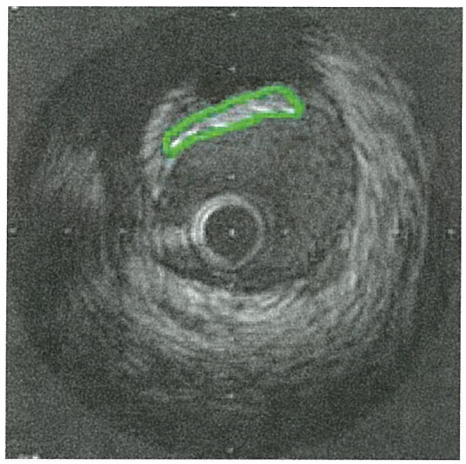

Figure 9. Manually defined calcium

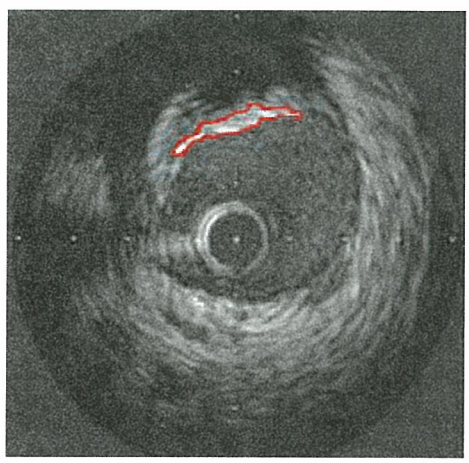

Figure 10. Automatic detection of calcium

G. Attenuation Imaging

The assumption that the total power of transmitted ultrFigure 11 is a conventional IVUS image and Figure 12 is the attenuation imaging of the same region. Guidewire shadow at 11 o'clock is compensated in attenuation imaging. The vein is clearly shown in the attenuation imaging while is is not obvious in the conventional IVUS imaging.

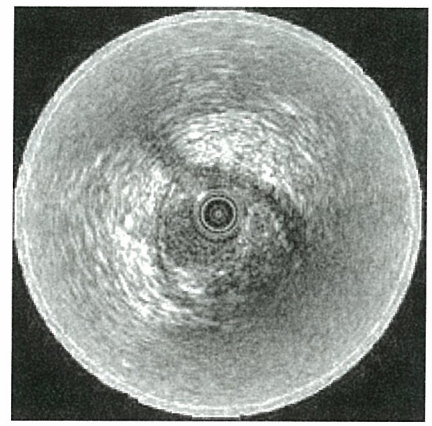

Figure 11. Conventional IVUS image

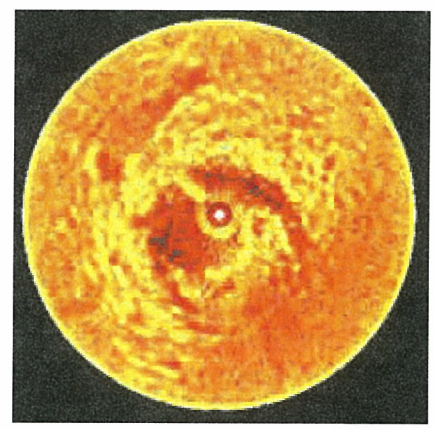

Figure 12. Attenuation imaging of the same region

IV. Conclusions

The evaluation of vulnerable plaque by multiple parametric IVUS analyses provides important information for assessment of acute coronary syndrome.

Acknowledgment

This study was supported by Grants-in-Aid for Scientific Research (Scientific Research (B) 13557059, 15300178) from the Japan Society for the Promotion of Science, Health and Labor Sciences Research Grants from the Ministry of Health, Labor and Welfare for the Research on Advanced Medical Technology (H17-Nano-001) and The Grant on Three Dimensional Organ Regeneration Program from New Energy and Industrial Technology Development Organization.

REFERENCES

[1] Saijo Y, Tanaka A, Owada N, Akino Y, Nitta S. Tissue velocity imaging of coronary artery by rotating-type intravascular ultrasound. *Ultrasonics*, Vol. 42, No. 1-9, 753-757, 2004.

[2] Saijo Y, Tanaka A, Iwamoto T, Dos Santos Filho E, Yoshizawa M, Hirosaka A, Kijima M, Akino Y, Hanadate Y, Yambe T. Intravascular two-dimensional tissue strain imaging. *Ultrasonics*. 2006 Jul 5; [Epub ahead of print]

[3] Iwamoto T, Tanaka A, Saijo Y, Yoshizawa M. Coronary plaque classification through intravascular ultrasound radiofrequency data analysis using self-organizing map. *Proc 2005 IEEE International Ultrasonics Symposium*, 2054-2057, 2005.

[4] Nair A, Kuban BD, Tuzcu EM, Schoenhagen P, Nissen SE, Vince DG. Coronary plaque classification with intravascular ultrasound radiofrequency data analysis. *Circulation*.Vol. 106, No. 17, 2200-6, 2002.

Development of Cerebella Tissue of Rat Characterized by Acoustic Impedance Microscope

N.Hozumi
Aichi Inst. of Technology
Toyota, Japan
hozumi@aitech.ac.jp

A. Kimura, S. Terauchi, M. Nagao, S. Yoshida
Toyohashi Univ. of Technology
Toyohashi, Japan

K. Kobayashi
Honda Electronics Co., Ltd.
Toyohashi, Japan

Y. Saijo
Tohoku Univ.
Sendai, Japan

***Abstract*— Acoustic microscopy is expected to be a powerful tool for observing biological matters without chemical staining. We have proposed a new method for two-dimensional acoustic impedance imaging for biological tissue that can perform micro-scale observation without preparing a sliced specimen. A tissue was attached on a 0.5 mm-thick plastic substrate. An acoustic pulse was transmitted from the rear side of the substrate. The reflection intensity was interpreted into local acoustic impedance of the target tissue. In the previous report, we demonstrated the outline of the system and the result of preliminary observation, showing its feasibility. This report deals with the optimization of the observation method, and characterization of the tissue of developing cerebellum. The result shows that change in acoustic impedance of each cerebellar layer depending on postnatal day was correspond to change of structure with growth.**

Keywords: biological tissue; acoustic impedanc; micro-scale imaging.

I. INTRODUCTION

Optical microscopy of biological tissue is generally taken after slicing and staining the tissue. This is destructive both mechanically and chemically. In addition, it needs relatively long time for staining process. On the contrary, acoustic imaging can be performed without staining process; i.e., it is chemically non-destructive. The observation can be finished in a very short time, as it does not need staining process. The idea of ultrasonic microscopy for biological tissue is based on this advantage, and it is considered to become a powerful tool for tissue characterization that can image elastic parameters.

Most of ultrasonic microscopes are scanning type, in which the response to a focused acoustic signal is successively acquired as the beam is mechanically scanned[1,2].The authors previously proposed a pulse driven ultrasonic sound speed microscopy that can obtain sound speed image in a short time [3,4]. Although a small roughness of the specimen was approved in this type of microscope, slicing the specimen into several micrometers was still required for the observation. However it is often required that the observation can be performed without slicing process, as slicing may damage some functions of a tissue.

Based on the above background, the authors have proposed the acoustic impedance microscopy that can image the local distribution of cross-sectional acoustic impedance of tissue[5]. As acoustic impedance is given as a product of sound speed and density, it would have a good correlation with sound speed, when the variance in density was not significant. In the previous report, the methodology of micro-scale imaging of cross-sectional acoustic impedance and its accuracy was described, showing its feasibility. In this report, the efforts to upgrade the image quality are dealt with. Thanks to these effort, a satisfactory clearness and precision of the image was realized. As an example, the change in postnatal day of each layer of cerebellum tissue of a rat was quantitatively characterized.

II. SAMPLE PREPARATION

The cerebellum tissue of a rat was employed as the specimen to be observed. Rats were dissected and removed their whole brains. To role out the effects of cross linker on the identification of neuronal structures by their acoustic impedance, we observed fresh cerebella organs without any chemical fixation. A sagittal cross section was exposed by a rotor slicer (Dohan EM, Kyoto, Japan). The specimen was rinsed and preserved in the same phosphate buffer solution (PBS). For optical observation, some adjacent slices were subjected to immunohistochemical staining against calbindin D-28k.

III. EXPERIMENTAL SETUP

Figure 1 illustrates the outline of the acoustic impedance microscope [5,6]. The tissue was attached on a 0.5 mm-thick plastic substrate. Distilled water was used as a coupling medium between the substrate and transducer. A sharp electric pulse of about 40 V in peak voltage and 2 ns in width was generated by the pulse generator (AVTEC, AVP-AV-HV3-C). The transducer was PVDF-TrFE type. An acoustic wave with a wide frequency range was generated by applying the voltage pulse. The acoustic wave, being focused on the interface between the substrate and tissue, was transmitted and received by

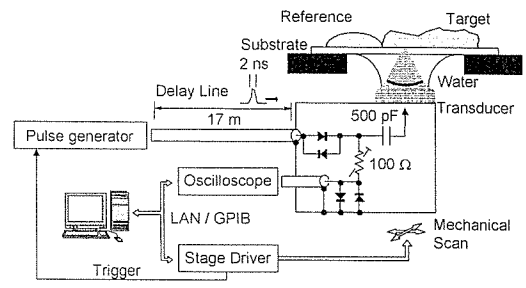

Fig.1 Schematic diagram of the system.

the same transducer. Considering the focal distance and the sectional area of the transducer, the diameter of the focal spot was estimated as about 40 μm at 80 MHz.

The substrate was a flat plastic plate made of polymethylmetacrylate (PMMA), its thickness being 0.5 mm. In order to retain hydrophilic property of the substrate, the surface was subjected to a plasma treatment using Keyence ST-7000. A reference material, of which acoustic impedance was known, was also placed on the same substrate. In many cases, the target tissue was observed together with the reference, by including it in the same field of view. In this series of experiment, we used pure water or a silicone rubber as the reference material. The substrate pasted with the rubber was preserved more than 12 hours after the rubber had been cured.

The reflection was detected and digitized by the oscilloscope (Tektronix, TDS-7145B). Two-dimensional profile of acoustic impedance was obtained by mechanically scanning the transducer. A typical field of view of 4 mm x 4 mm was covered with 200 x 200 pixels. It took typically 2 - 3 minutes for one observation. All the measurements were performed at room temperature.

The target signal is compared with the reference signal and interpreted into acoustic impedance as

$$Z_{target} = \frac{1-\frac{S_{target}}{S_0}}{1+\frac{S_{target}}{S_0}} Z_{sub} = \frac{1-\frac{S_{target}}{S_{ref}} \cdot \frac{Z_{sub}-Z_{ref}}{Z_{sub}+Z_{ref}}}{1+\frac{S_{target}}{S_{ref}} \cdot \frac{Z_{sub}-Z_{ref}}{Z_{sub}+Z_{ref}}} Z_{sub}$$

where S_0 is the transmitted signal, S_{target} and S_{ref} are reflections from the target and reference, Z_{target}, Z_{ref} and Z_{sub} are the acoustic impedances of the target, reference and substrate, respectively [5,6].

In case of using water as the reference, its acoustic impedance was assumed to be 1.5 x 10^6 Ns/m^3. On the other hand, in case of using silicon rubber, the acoustic impedance of itself was calibrated, by using water as the standard reference material. In this report, 0.965 x 10^6 Ns/m^3 was used. The acoustic impedance of the substrate was calculated to be 3.22 x 10^6 Ns/m^3,considering its sound speed and density.

IV. RESULTS AND DISCUSSION

A. Observation of cerebellar cortex of a rat

Figure 2 illustrates the development of cerebellar cortex. In immature cerebellum, structure of layer is not clear, but in mature cerebellum, 4 layers are visible; molecular layer (ML), Purkinje layer (PL), internal granular layer (IGL) and white matter (WM). Parallel fibers in ML are axon of granule cells and play an important role in cerebella neural connection. Migrating granule cells elongate them horizontally and form a lot of excitatory synapses to dendrite of Purkinje cells. These are major neuronal circuits of cerebellum so that parallel fibers are expected to construct rich ML with development.

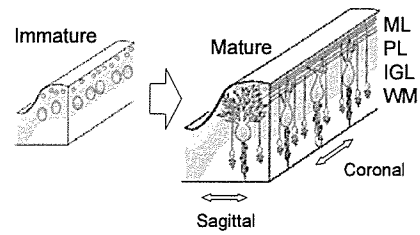

Fig. 2 Illustration of development of cerebellar cortex.

In order to upgrade the clearness and precision of the acoustic impedance image, we took following two countermeasures;

(1) Surface of the substrate was treated with plasma to upgrade hydrophilic property.
(2) The specimen was kept in humid condition during the measurement, using a protection cover mounted on the substrate.

B. Plasma treatment

The PMMA substrate was chosen, as it has a good accuracy of dimension and acoustic transmittance. However, its hydrophilic property is not sufficient, leading to a poor contact between the substrate and tissue. Figure 3 shows the images with and without plasma treatment for the substrate surface. The images were taken from the rats of the same postnatal day.

In image (a), although the layers close to the boundary between the tissue and outside (the part that looks black in the image) are clearly seen, those inside the tissue are not clear. This would be due to a coupled water layer to the tissue on the substrate. In order to improve the contact by upgrading hydrophilic property, a plasma treatment was performed prior to the observation. After plasma treatment, a contact angle to water reduced from 55 degrees to 39 degrees. Surface energy after plasma treatment would be increased, bringing about a better hydrophilic property. As its good hydrophilic property is kept for about one hour, the observation was completed within one hour after the treatment. As shown in image (b), the internal structure is clearly seen when the treatment was performed.

In order to quantitatively assess the effect of plasma treatment, the acoustic impedance through the same layer was traced. Figure 4 shows the examples. Each trace was performed along the white line indicated in Figure 3. The acoustic impedance of ML, as its fine structure made with a fat sheath

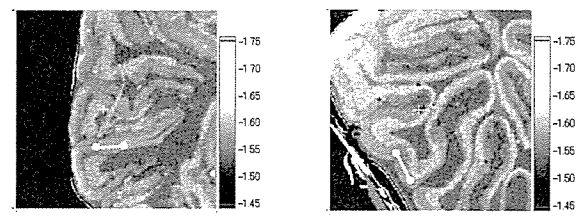

(a) not treated (b) treated

Fig.3 Effect of plasma treatment.

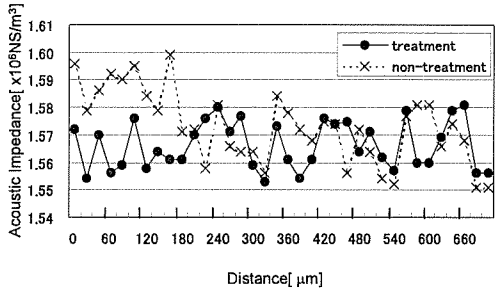

Fig.4 Change of acoustic impedance along the white line indicated in Fig. 3.

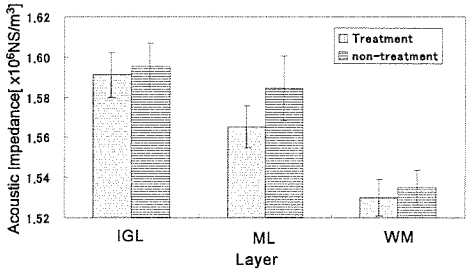

Fig. 5 Acoustic impedance of each layer with and without plasma treatment.

of myelin is far less than the scale of focal spot, should be uniformly observed. However as shown in the figure, a significant difference in dispersion is seen depending on the surface condition of the substrate. It is obvious that the ML is observed with more uniform acoustic impedance by treating with plasma.

Figure 5 shows the acoustic impedance of each layer with and without plasma treatment. Each bar represents the average of 400 points, the length of error bar indicating twice the standard deviation. Plasma treatment does not seem to affect the acoustic impedance of IGL and WM, both in average and standard deviation.

On the other hand, in case of ML, there is a difference of 0.022×10^6 Ns/m^3 in average acoustic impedance, as well as a significant difference in standard deviation. This would result from the structure of each layer. A lot of fine fibers are assembled in ML, whereas both WM and IGL are formed from coherent large cells. An ML fiber, 0.2 micrometers in diameter, is much smaller than the cell scale of WM and IGL ranging from ten to a few tens of micrometers. Cell surface shows both hydrophilic and hydrophobic properties, though it is coupled with hydrating water molecules in solution. Most cells could contact with the hydrophobic substrate without hydrating water. Even if the substrate gets more hydrophilic property by plasma treatment, large cells composing WM and IGL could exclude surface water, leading to a relatively firm contact with the substrate. Therefore acoustic impedance of these layers did not show a significant variation depending on the plasma treatment.

However, in the case of ML, the fine fibers might be too small to tightly contact with the substrate. When the substrate acquires hydrophilic property, water could move thorough the ML and form a water-rich layer in contact with the substrate. Therefore the ML on the substrate after plasma treatment would indicate a lower acoustic impedance, reflecting the low acoustic impedance of water. Furthermore, this water-rich layer would bring about relatively low standard deviation in acoustic impedance compared with the case without the plasma treatment.

C. Prevention from dry out

The tissue specimen tend to dry out, leading to higher acoustic impedance. Figure 6 (a) shows this problem. The images of the tissue observed shortly after the preparation is shown in the left side. When the specimen had been exposed to the air with 22 % of relative humidity at 38 C for 20 minutes, the image was significantly changed as shown in the left side image. In order to prevent the dry out, a protection cover, as shown in Fig. 7, was mounted on the substrate after sample preparation. As shown in image (b), the change of image due to dry out was sufficiently prevented by applying the protection cover.

In order to confirm its effectiveness, a droplet of 2 wt% saline solution was subjected to the observation at 23 C in 56 % of ambient relative humidity, using pure water as the reference.

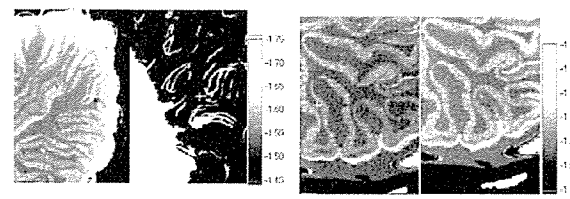

(a) without cover (b) with cover

Fig.6 Acoustic impedance images shortly after mounting the tissue on the substrate (left) and 20 minutes later (right).

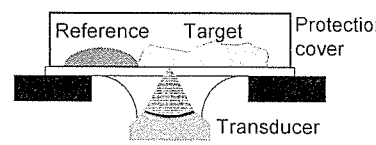

Fig.7 A protection cover mounted on the substrate.

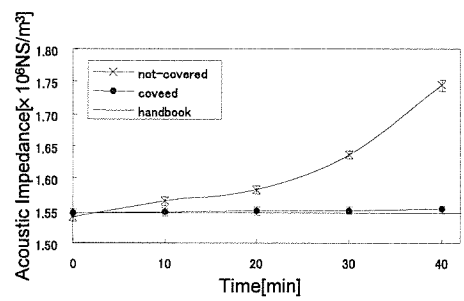

Fig.8 Change in time of acoustic impedance of saline droplet placed on the substrate. Initial content of NaCl was 2 wt%.

Figure 8 shows the result. Each plot represents the average of 900 points, the length of error bar indicating twice the standard deviation. The dotted line represents the acoustic impedance calculated from the handbook data. In case without the cover, due to concentration, the change of impedance is not negligible at 10 minutes, and it reaches as high as 1.75 x 10^6 Ns/m^3 at 40minuites. This change is not erroneous, as the precision of this measurement is proved to be as small as 0.006 x 10^6 Ns/m^3[5]. On the contrary, in case with the protection cover, the acoustic impedance is measured as a constant value not depending on time. It is supposed that the saturated humidity inside the cover successfully protected from dry out.

D. Acoustic impedance of each layer of cerebellum depending on its development

Figure 9 shows the observed images of cerebellar cortex of rat at immature (P1: postnatal 1 day), transient (P7 and P14), and mature (p21) stages. In the immature cerebellar cortex (P1), the external granular layer (EGL), the outer layer of the cortex, showed higher impedance than the inner layers. At this stage, many stiff granule cells compose EGL. In the inner layers, myelination is not yet progressed, and the existence of white matter is not clearly observed.

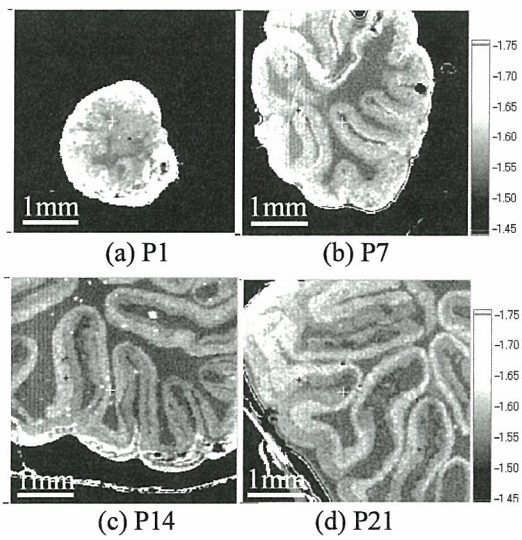

Fig.9 Two-dimensional profiles of acoustic impedance of cerebellar cortex.

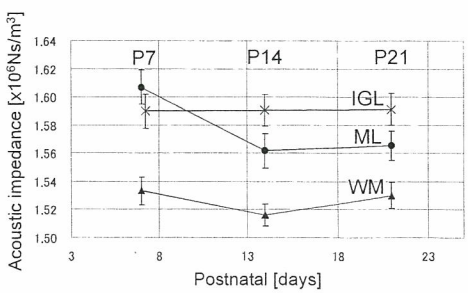

Fig. 10 Change of acoustic impedance of each layer as a function of postnatal day.

Over transient stage, four different layers are clearly observed. As shown in Fig. 10, acoustic impedance of ML indicated higher value once in P7, but it decayed through the growth up to P14. The IGL is kept at high impedance, and the WM is kept at low. It is suggested that migrating granule cells in ML lead to a high impedance in P7, and relatively stable impedances of IGL and WM would be reflected from the stable properties of these layers.

V. CONCLUSIONS

Acoustic impedance microscope for biological tissue characterization was proposed. It can perform the observation neither staining nor slicing the specimen. Two measures to upgrade the image quality were taken. Plasma treatment improved the hydrophilic property of the substrate surface. Protection cover was proved to keep the specimen in good condition for observation. A quantitative assessment of acoustic impedance of each layer of cerebellar tissue in the development process of a rat was performed without chemical fixation. IGL and WM showed relatively stable value, whereas a significant change as a function of postnatal day was seen with ML. The change in acoustic impedance of ML would be reflecting the development of parallel fiber structure.

ACKNOWLEDGEMENTS

The authors would like to express their sincere thanks to T. Morishima and E. Fukushi of Toyohashi University of Technology for their assistance with the experiment. This study was financially supported by Grants-in-Aid for Scientific Research (Scientific Research (B)18360196), and Japan Society for the Promotion of Science and Health and Labor Sciences Research Grants from the Ministry of Health, Labor and Welfare for the Research on Advanced Medical Technology (H17-Nano-001).

REFERENCES

[1] Y. Saijo, M. Tanaka, H. Okawai, H. Sasaki, S. Nitta & F. Dunn: "Ultrasonic Tissue Characterization of Infarcted Myocadium by Scanning Acoustic Microscopy", *Ultrasound in Med. & Biol.*, 23-1, 77 (1997).

[2] H. Okawai, K Kobayashi & S. Nitta: "An Approach to Acoustic Properties of Biological Tissues Using Acoustic Microgfraphs of Attenuation Constant and Sound Speed", *J. Ultrasound Med.*, 20, 891 (2001).

[3] N. Hozumi, R. Yamashita, C-K Lee, M. Nagao, K. Kobayashi, Y. Saijo, M. Tanaka, N. Tanaka & S Ohtsuki: "Ultrasonic Sound Speed Microscope for Biological Tissue Characterization Driven by Nanosecond Pulse", *Acoustic Science & Technology*, 24, 386 (2003).

[4] N. Hozumi, R. Yamashita, C-K. Lee, M. Nagao, K. Kobayashi, Y. Saijo, M. Tanaka, N. Tanaka & S.Ohtsuki: "Time –frequency analysis for pulse driven ultrasonic microscopy for biological tissue characterization", *Ultrasonics*, 42, 717 (2003).

[5] N. Hozumi, A. Kimura, S. Terauchi, M. Nagao, S. Yoshida, K. Kobayashi & Y. Saijo: "Acoustic Impedance Micro-imaging for Biological Tissue Using a Focused Acoustic Pluse with a Frequency Range Up to 100 MHz" IEEE International Ultrasonics Symposium, pp170-173 (2005).

[6] A. Kimura, N. Hozumi, S. Terauchi, M. Nagao, S. Yoshida, K. Kobayashi & Y. Saijo: "Imaging for Biological Tissue with Acoustic Impedance Microscope", 8th sendai symposium on Ultrasonic Tissue Characterization (2005).